Journal of Nuclear Medicine, published on June 16, 2022 as doi:10.2967/jnumed.122.263977

Evaluation of (*rac*)-, (*R*)- and (*S*)-^{18}F-OF-NB1 for imaging GluN2B subunit-containing *N*-methyl-*D*-aspartate receptors in non-human primates

Hazem Ahmed[1, 2*], Ming-Qiang Zheng[2*], Kelly Smart[2], Hanyi Fang[2, 3], Li Zhang[2], Paul R. Emery[2], Hong Gao[2], Jim Ropchan[2], Ahmed Haider[1], Gilles Tamagnan[2], Richard E. Carson[2], Simon M. Ametamey[1†], Yiyun Huang[2†]

1. Institute of Pharmaceutical Sciences, ETH Zurich, Zurich, Switzerland

2. PET Center, Yale University, New Haven, Connecticut, USA

3. Union Hospital, Huazhong University of Science and Technology, Wuhan, China

* Both authors contribute equally to this work

First author: Dr. Hazem Ahmed, Institute of Pharmaceutical Sciences, ETH Zurich, Zurich, Switzerland.

e-mail: hazem.ahmed@pharma.ethz.ch

†Corresponding authors

- Prof. Yiyun Henry Huang, PO Box 208048, PET Center, Yale School of Medicine, 801 Howard Ave, New Haven, CT 06520-8048, USA, Tel: 203-785-3193, e-mail: henry.huang@yale.edu
- Prof. Simon M. Ametamey, Institute of Pharmaceutical Sciences, ETH Zurich, Zurich, Switzerland e-mail: simon.ametamey@pharma.ethz.ch

Word count: 4954

Short running title: PET imaging of GluN2B-NMDA in monkeys

This study was funded by the National Institute of Health (Grant U01MH107803) and also partly supported by the Swiss National Science Foundation (Grants numbers 310030E-160403/1 and 310030E-182872/1).

ABSTRACT

Despite two decades of research, no GluN1/2B radioligand is yet clinically validated. Previously, we reported on (*rac*)-^{18}F-OF-NB1 as a promising GluN1/2B PET probe in rodents, and its successful application for the visualization of GluN2B-containing *N*-methyl-D-aspartate receptors (NMDARs) in postmortem brain tissues of patients with amyotrophic lateral sclerosis. In the current work, we report on the *in vivo* characterization of (*rac*)-, (*R*)- and (*S*)-^{18}F-OF-NB1 in non-human primates.

Methods PET scans were performed in rhesus monkeys. Plasma profiling was used to obtain the arterial input function. Regional brain time-activity curves (TACs) were generated and fitted with the one-tissue and two-tissue compartment models (1TCM and 2TCM) and the multilinear analysis-1 (MA1) method, and the corresponding regional volumes of distribution (V_T) were calculated. Blocking studies with the GluN1/2B ligand Co 101244 (0.25 mg/kg) were performed for the enantiopure radiotracers. Receptor occupancy, non-specific volume of distribution, and regional binding potential (BP_{ND}) values were obtained. Potential off-target binding towards sigma-1 receptors (σ1Rs) was assessed for (*S*)-^{18}F-OF-NB1 using the σ_1R ligand FTC-146.

Results Free plasma fraction was moderate, ranging from 12% to 15%. All radiotracers showed high and heterogeneous brain uptake with highest levels in the cortex. (*R*)-^{18}F-OF-NB1 showed the highest uptake and slowest washout kinetics out of all tracers. The 1TCM and MA1 method fitted the regional TACs well for all tracers and produced reliable regional V_T values, which were higher for (*R*)- than (*S*)-^{18}F-OF-NB1. Receptor occupancy by Co 101244 was 85% and 96% for (*S*)-^{18}F-OF-NB1 and (*R*)-^{18}F-OF-NB1, respectively. Pretreatment with FTC-146 at both a low (0.027 mg/kg) and high (0.125 mg/kg) dose led to similar reduction (48% and 49%, respectively) in specific binding of (*S*)-^{18}F-OF-NB1. Further, pretreatment with both Co 101244 and FTC-146 did not result in further reduction of specific binding than Co 101244 alone in the same monkey (82% vs 81%, respectively). *R*egional BP_{ND} values ranged from 1.32 in the semiovale to 3.44 in the cingulate cortex for (*S*)-^{18}F-OF-NB1.

Conclusion Both (*R*)- and (*S*)-^{18}F-OF-NB1 exhibited high binding specificity to GluN2B subunit-containing NMDARs. The fast washout kinetics, good regional BP_{ND} values, and high plasma free fraction render (*S*)-^{18}F-OF-NB1 an attractive radiotracer for clinical translation.

Keywords NMDA, GluN2B subunit, Brain PET Imaging, Non-human Primates, Neurodegeneration

INTRODUCTION

Glutamatergic *N*-methyl-D-aspartate receptors (NMDARs) are heterotetrameric ion channels ubiquitously expressed in the mammalian brain. The receptor complex is assembled from distinct subunits, namely GluN1(a-h), GluN2(A-D) and GluN3(A-B) where each GluN2 subtype exhibits a unique spatiotemporal expression and function (*1*). NMDARs are known to be the linchpin for synaptic plasticity and transmission as well as higher cognitive functions. Notably, synaptic NMDARs are promotors of cell survival whereas extrasynaptic GluN2B subunit-enriched NMDARs are mediators of cell death. The GluN1/2B receptors are associated with several neuropathologies such as Alzheimer's disease, Parkinson's disease, depression, schizophrenia and stroke amongst others (*2-5*). As such, the development of GluN1/2B antagonists has been the prime focus of therapeutic development efforts over the past two decades, where 19 therapeutic patent applications have been published in the past five years alone (*6,7*). Although these subtype selective antagonists possess pharmacological action similar to conventional NMDA ion channel blockers, they exhibit a much more favorable neurological safety profile, as their selectivity is thought to preserve the physiological functions of NMDA receptors but minimize potential undesired pharmacological effects (*4,8*). To date, several GluN1/2B antagonists such as CERC-301 have been evaluated in clinical trials with no-to-modest clinical benefits, while others are still in development (*7,9*). Positron emission tomography (PET) imaging is a powerful modality that can accelerate drug development, for example, to be used in target engagement and drug occupancy studies, and as a credible tool in patient selection and monitoring (*10,11*). Despite the long-standing interest, efforts to develop a GluN1/2B-specific PET radioligand have largely been unsuccessful. Challenges include poor brain uptake, homogenous distribution and existence of brain radiometabolite(s), as well as binding to other brain receptors, most notably sigma-1 receptors (σ_1Rs) (*12*).

The 3-benzazepine structural class of compounds has recently emerged as potential PET radioligand candidates for the imaging of GluN1/2B (Figure 1) (*13,14*). Recently, Ametamey and co-workers successfully developed the 3-benzazepin-1-ol derivative, (*R*)-^{11}C-Me-NB1, for imaging GluN1/2B

in humans (*15-17*). To overcome the short physical half-life limitation for ^{11}C-labelled radioligands, we evaluated several radiofluorinated derivatives in animals (*18-20*). (*Rac*)-^{18}F-OF-NB1 (K_i (GluN1/2B) = 10.4 ± 4.7 nM) emerged as one of the most promising candidates for evaluation in non-human primates (NHPs) (*19*). In the current work and for the purpose of clinical translation, we evaluated the pharmacokinetic and imaging properties of (*rac*)-, (*S*)-, (*R*)-^{18}F-OF-NB1 in NHPs, and performed a comprehensive assessment of (*S*)-^{18}F-OF-NB1 regarding its binding specificity to GluN1/2B receptors and selectivity over σ_1Rs *in vivo*.

MATERIALS AND METHODS

Chemistry

Synthesis of the reference compound (*rac*)-OF-NB1 and the corresponding aryl boronic ester precursors as well as their chiral High Performance Liquid Chromatography (HPLC) separation followed previously published procedures (*18,19*).

Radiochemistry

^{18}F-Fluoride was produced via the ^{18}O(p.n)^{18}F nuclear reaction using $H_2{}^{18}O$ (Huayi Isotopes, Toronto, Canada) in a 16.5 MeV GE PETtrace cyclotron (Uppsala, Sweden). After bombardment, the activity was transferred to a shielded hotcell, and trapped on an anionic exchange resin cartridge (Chromafix PS-HCO_3, Macherey-Nagel, Dueringen, Germany). Trapped $^{18}F^-$ was eluted into a sealed 5 mL borosilicate glass reaction vial using 2 mL solution of $K_2C_2O_4$ (1.0 mg/mL in water), K_2CO_3 (0.1 mg/mL in water), and Kryptofix 222 (6.3 mg/mL in acetonitrile). The solution was azeotropically dried for 5 min at 110 °C under nitrogen, followed by 2 x drying using 0.4 mL acetonitrile each. Afterwards, the vial was purged with 20 mL of air prior to the addition of 0.4 mL of the boronic ester precursor solution (6 mg of precursor and 12 mg of $Cu(OTf)_2(Py)_4$ in anhydrous dimethylacetamide). The reaction mixture was stirred at 110 °C for 20 min, diluted with 10 mL of deionized water, and passed through a Waters C18 SepPak cartridge (Milford,

MA, USA). The cartridge was washed with 10 mL deionized water. The trapped activity was eluted from the SepPak with 1 mL ethanol into a second reaction vial. The solvent was dried at 90 °C under nitrogen stream. Dichloromethane and anhydrous BBr_3 were added, and left to react for 15 min at room temperature. The solvent was removed by gentle nitrogen blowing and the crude product re-dissolved in the HPLC mobile phase (25% acetonitrile/ 75% 0.1 M ammonium formate with 0.5% acetic acid, pH=4.2). The solution was injected into a semi-preparative HPLC system equipped with an Agilent Eclipse XDB-C18 (9.4 x 250 mm, 5 μm) column eluting with the above mobile phase at a flow rate of 5 mL/min. The radioactive peak from 15 to 16 min was collected and diluted with 50 mL of water. The solution was passed through a Waters C18 SepPak cartridge. The product was eluted from the SepPak with 1 mL of ethanol and dried under gentle nitrogen blowing. The product was re-dissolved with the second HPLC mobile phase (32% acetonitrile/68% water with 0.05% triethylamine) and injected into the chiral semi-preparative HPLC system equipped with a Regis reflect I-Amylose A column (250 x10 mm, 5 μm) eluting with the aforementioned mobile phase at a flow rate of 5 mL/min. The radioactive peaks corresponding to (*R*)-^{18}F-OF-NB1 (eluting from 23 to 25 min) and (*S*)-^{18}F-OF-NB1 (eluting from 27 to 29 min) were collected in two separate bottles, and diluted with 50 mL of water each. The solutions were passed through Waters C18 SepPak cartridges separately. Each SepPak was washed with 1 mM HCl (10 mL), dried with air, then eluted with 1 mL of USP ethanol, followed by 3 mL of USP saline, into a collection vial. The solution was then passed through a 0.22 μm GV filter (Millipore, Sigma) into a 10 mL dose vial pre-charged with 7 mL of USP saline for formulation.

Measurement of Lipophilicity (log $D_{7.4}$)

Lipophilicity (log $D_{7.4}$) of (*S*)-^{18}F-OF-NB1 was determined according to previously published procedures (*21*,*22*). The log $D_{7.4}$ was calculated as the ratio between the concentrations of decay-corrected radioactivity in 1-octanol and pH 7.4 phosphate buffered saline (Dulbecco).

PET Imaging in Rhesus Monkeys

All experimental procedures were approved by the Yale University Institutional Animal Care and Use Committee. A total of eleven dynamic PET scans (120 min duration each) were performed in three rhesus monkeys (Macaca mulatta, 2 males and 1 female) on the Focus 220 scanners (Siemens Medical Solutions, Knoxville, TN, USA).

Baseline scans were acquired for (*rac*)-, (*R*)-, and (*S*)-^{18}F-OF-NB1 whereas blockade scans using the GluN1/2B antagonist Co 101244 (0.25 mg/kg, IC_{50} = 4±1 nM for GluN1/2B) were performed for the enantiopure radiotracers (*23*). Further, blockade scans using either the σ_1R antagonist FTC-146 (two doses; 0.027 and 0.125 mg/kg, K_i = 0.0025 nM for σ_1R) alone or GluN1/2B (0.25 mg/kg of Co 101244) followed by σ_1R blockade (0.125 mg/kg of FTC-146), were accomplished using (*S*)-^{18}F-OF-NB1 (*24*). Procedures for PET scanning, image processing and analysis are detailed in the supplemental information.

Arterial Input Function Measurement and Metabolite Analysis. Plasma activity and parent fraction determination were performed in accordance to previously published procedures (*25*,*26*). Radioactivity was measured in whole blood and plasma from arterial samples taken at various time points after radiotracer injection using cross-calibrated gamma counters (Wizard 1480/2480, Perkin Elmer, Waltham, MA, USA). Radiometabolic profile was investigated by HPLC analysis using a column-switching method with plasma samples from 0, 5, 15, 30, 60, 90 and 120 min after radiotracer injection (*27*). The patent fraction was calculated as the ratio of the radioactivity in parent compound-containing fractions to the total radioactivity measured. Finally, the arterial input function was calculated as the product of total plasma concentrations and the interpolated parent fraction at each time point.

Measurement of Radiotracer Free Fraction in Plasma (f_p). Ultrafiltration was the method of choice for measuring the unbound radiotracer in plasma f_p (*28*). The f_P measurement was carried out in triplicates

per scan, and defined as the ratio of the radioactivity concentration in the filtrate to the total activity in plasma.

*Kinetic modeling***.** The regional time-activity curves (TACs) and metabolite-corrected arterial input functions were analyzed with the one- and two-tissue compartment model (1TCM and 2TCM), as well as the multilinear analysis 1 (MA1) method (starting time of 30 min) to calculate the kinetic parameters (*28*). Regional volume of distribution (V_T, mL/cm^3) from each model was derived and compared. Target occupancy and the non-displaceable volume of distribution (V_{ND}) in the brain was derived from the Lassen plot, generated using the baseline regional V_T values and the V_T difference between baseline and blockade scans (*29*). Regional binding potential (BP_{ND}) was calculated as $BP_{ND} = (V_T - V_{ND})/V_{ND}$ using the V_{ND} value derived from the Lassen plot for the GluN1/2B blocking scan.

RESULTS

Chemistry

The overall chemical yields of the reference compounds (*rac*)-, (*S*)-, (*R*)-OF-NB1, and the respective boronic ester precursors were comparable to those published previously (*18,19*).

Radiochemistry

The radiosynthetic strategy is depicted in Figure 2. Despite starting from enantiopure precursors, racemization occurred during the deprotection step, requiring additional chiral purification. The final activity obtained were 1480 ± 185 MBq (n=5) for (*rac*)-^{18}F-OF-NB1 and 203.7 ± 81.4 MBq (n=10) for (*S*)- and (*R*)-^{18}F-OF-NB1, respectively. The radiotracers were prepared in >99% radiochemical purity. (*S*)- and (*R*)-^{18}F-OF-NB1 were both obtained in >98% enantiomerical purity. Molar activity was 143.5 ± 127.3

GBq/μmol (n= 10) at the end of synthesis. Total synthesis time for (*S*)- and (*R*)-^{18}F-OF-NB1 was 200 min on average.

Measurement of log $D_{7.4}$

The measured log $D_{7.4}$ of (*S*)-^{18}F-OF-NB1 was 2.05 ± 0.08 (n = 4), similar to the log $D_{7.4}$ of (*rac*)-^{18}F-OF-NB1, and in the optimal range for brain penetration (*19*,*30*).

PET Imaging Experiments in Rhesus Monkeys

The amount of injected radioactivity and associated mass was 147.1 ± 47.4 MBq and 1.05 ± 0.70 μg (n = 10). The parent fractions at 30 min post-injection were 33% (n=2), 32% (n=2) and 57% (n=1), respectively, for the baseline scans of (*rac*)-, (*S*)- and (*R*)-^{18}F-OF-NB1 (Figure 3). For both (*S*)- and (*R*)-^{18}F-OF-NB1, the parent fractions decreased to 26% (n=2) and 27%, respectively, after pretreatment of the animals with the GluN1/2B antagonist Co 101244, while pre-blocking with the σ_1R antagonist FTC-146, whether at low or high dose, did not change the parent fraction of (*S*)-^{18}F-OF-NB1 (32%). The f_P was 0.12 ± 0.01 for (*rac*)-^{18}F-OF-NB1 (n = 2), 0.16 ± 0.01 for (*S*)-^{18}F-OF-NB1 (n = 8), and 0.13 for (*R*)-^{18}F-OF-NB1 (n = 1).

In the monkey brain, all tracers showed heterogeneous distribution; with high uptake in the cortex, putamen, and cerebellum, moderate in the hippocampus and thalamus, and lowest in the centrum semiovale (Figure 4). Brain uptake of (*S*)-^{18}F-OF-NB1 peaked at standardized uptake value (SUV) of 4-5 within 20 min post-injection, followed by a relatively fast clearance. The (*R*)-enantiomer, on the other hand, displayed slow brain clearance, with uptake increasing throughout the 120 min scan time. Brain uptake levels and tissue clearance of (*rac*)-^{18}F-OF-NB1 were between those of the two enantiomers (Supplemental Figure 1). Pretreatment with the GluN1/2B antagonist Co 101244 (0.25 mg/kg) reduced radioactivity levels in all

regions to nearly those in the semiovale for both enantiomers at the end of the scans. Receptor occupancy by 0.25 mg/kg Co 101244 was estimated at 81% and 88% across the brain in two separate monkeys for (*S*)-^{18}F-OF-NB1, and 96% for (*R*)-^{18}F-OF-NB1 (Figure 5). Pre-treatment with a σ_1R antagonist reduced the uptake of (*S*)-^{18}F-OF-NB1 across all brain regions. Low (0.027 mg/kg) and high doses (0.125 mg/kg) of FTC-146 reduced the specific binding of (*S*)-^{18}F-OF-NB1 by 48% and 49%, respectively. Double blocking with sequential administration of both Co 101244 (0.25 mg/kg) and high dose FTC-146 (0.125 mg/kg) in one monkey at 25 and 15 min prior to the radiotracer injection, respectively, did not result in further reduction in brain uptake of (*S*)-^{18}F-OF-NB1 when compared to blocking with Co 101244 alone (82% vs 81%).

The TACs were well fitted with both the 1TCM and MA1 method for reliable V_T estimates with relative standard error of <5% (Supplemental Tables 1 and 2). On average V_T values were similar for (*rac*)- and (*R*)-^{18}F-OF-NB1, and lower for (*S*)- ^{8}F-OF-NB1. Regional V_T values ranged from 17 to 39 mL/cm^3 for (*S*)-^{18}F-OF-NB1 in the selected brain regions (Table 1). From the GluN1/2B blocking studies, V_{ND} was found to be 9.3 mL/cm^3 for (*S*)-^{18}F-OF-NB1 in monkey#1 and 7.3 mL/cm^3 in monkey#2. Based on these V_{ND} values, regional BP_{ND} values were calculated and ranged from 1.2 (semiovale) to 3.4 (cingulate cortex) for (*S*)-^{18}F-OF-NB1 (Table 1).

DISCUSSION

Given the involvement of GluN1/2B receptors in various neuropathologies, great strides have been taken to develop therapeutic and PET imaging agents, and several radioligands are currently in development. (*R*)-^{11}C-Me-NB1 was recently evaluated in healthy volunteers, and shown to have excellent brain uptake and kinetics (*17*). These results warrant the development of a radiofluorinated PET tracer that would allow a wider use. We have previously synthesized and tested several ligands, and (*rac*)-^{18}F-OF-NB1 emerged as one of the most promising candidates for clinical translation, given its excellent properties in rodents (*19*).

In the current work, we evaluated the performance characteristics of (*rac*)-^{18}F-OF-NB1 and its enantiopure (*S*)- and (*R*)-^{18}F-OF-NB1 with respect to their brain uptake, kinetics and metabolism, in order to select the most promising candidate for clinical translation. To our knowledge, there have been no reports of clinical trials on the evaluation of a radiofluorinated probe for PET imaging of GluN1/2B in humans.

The radiosynthesis of ^{18}F-OF-NB1 proceeded in two steps: copper-catalyzed radiofluorination of the boronic ester precursor, followed by simultaneous cleavage of the two hydroxyl protecting groups (*19*). Despite starting with enantiopure precursors, the respective enantiopure (*S*)- and (*R*)-^{18}F-OF-NB1 could not be obtained without racemization during the second deprotecting step. As such, the radiosynthetic strategy was adapted to include a chiral HPLC purification step to provide enantiopure radiotracers at the end of the synthesis (Supplemental Figure 2). This allowed the production of both enantiomers from a single radiosynthetic run. Metabolite analysis showed higher parent fraction in the plasma for (*R*)-^{18}F-OF-NB1 than the (*S*)-enantiomer. This phenomenon can be explained by the fact that different enantiomers can bind to enzymes with different affinities, and therefore exhibit different metabolic rates (*31*). Further, all forms of ^{18}F-OF-NB1 presented good f_p values (0.12-0.15), which offers the opportunity for high precision measurement, and subsequently improving the accuracy of quantitative PET measurements, and calculation of V_T/f_p, a potentially valuable outcome measure in clinical trials.

The brain uptake and distribution of (*rac*)-^{18}F-OF-NB1 corroborated results observed in rodents (*19*). Kinetic analysis, however, is not suited for racemic mixtures unless both enantiomers exhibit identical plasma clearance. The two enantiopure radiotracers displayed brain distribution and kinetics that are in line with the results in rodents. (*R*)- and (*S*)-^{18}F-OF-NB1 showed high uptake in GluN1/2B-rich brain regions, with the highest uptake in the cingulate cortex. The binding of both enantiopure tracers was displaceable across all brain regions, indicating the lack of a reference region for kinetic modeling analysis. Regional TACs of all three tracers, on the other hand, were well-fitted by the 1TCM. The 2TCM also produced reasonable model fits, but the standard error of V_T values was high and non-physiological values were generated in several grey matter regions. The MA1 method also provided good fits and V_T values

comparable to those derived from 1TCM (*32*). Regional V_T estimates were higher for (*R*)-^{18}F-OF-NB1 than the (*S*)-enantiomer. When plotting V_T values of (*R*)- and (*S*)-^{18}F-OF-NB1 against each other to generate the Guo plot (*33*), the slope of this curve indicated four to five-fold higher *in vivo* affinity for (*R*)-^{18}F-OF-NB1 than (*S*)-^{18}F-OF-NB1 (Figure 6).

To investigate the *in vivo* binding specificity of both enantiomers to GluN1/2B, blocking experiments with the GluN1/2B antagonist Co 101244 (0.25 mg/kg) were performed and a Lassen plot analysis for each enantiomer was undertaken. Both enantiomers showed high specific binding, with an estimated occupancy of 96% (n=1) across the brain by Co 101244 (0.25 mg/kg) when measured with (*R*)-^{18}F-OF-NB1, and 85% (n=2) with (*S*)-^{18}F-OF-NB1. Furthermore, both enantiomers exhibited good regional BP_{ND} values in the range of 2-3, highlighting their clinical translation potential in terms of specific binding (Table 1). The high affinity of (*R*)-^{18}F-OF-NB1 came at the expense of a less desirable pharmacokinetic profile due to its extremely slow washout from the brain, which precluded its further development, since a very long scan might be required in humans. Pretreatment with a low (0.027 mg/kg) or high dose (0.125 mg/kg) of the σ_1R antagonist FTC-146 led to a partial blocking with 49% and 48% reduction in the specific binding of (*S*)-^{18}F-OF-NB1, respectively, as calculated from the Lassen plots, with no clear dose-blockade level relationship. In order to address this potential "off-target" binding component of (*S*)-^{18}F-OF-NB1, a sequential blockade experiment was conducted where Co 101244 (0.25 mg/kg) was injected first, followed by the σ_1R antagonist FTC-146 (0.125 mg/kg). Blocking with 0.25 mg/kg Co 101244 alone resulted in 81% occupancy and virtually no change in occupancy was observed when FTC-146 was administered thereafter. The absence of further reduction in binding after treatment with FTC-146 suggests that (*S*)-^{18}F-OF-NB1 binds specifically to the GluN1/2B receptors and is selective over σ_1Rs. The partial blockade of (*S*)-^{18}F-OF-NB1 binding by FTC-146 when administered alone can be attributed to σ_1R-NMDAR cross-talk stemming from the inherent chaperone nature of σ_1Rs, and their ability to regulate the NMDARs (*34*,*35*). Another plausible explanation might be off-target binding of FTC-146, as the σ_1R bears a particular binding site that is structurally similar to the ifenprodil-binding site of the GluN1/2B receptor, and thus σ_1R ligands

are known for their off-target binding at the GluN1/2B. For example, we have reported potential off-target binding by the σ_1R ligand fluspidine (*19*). Nonetheless, further studies are warranted to clarify the nature of potential off-target binding by these novel benzazepinol-based radioligands.

CONCLUSION

We successfully synthesized and evaluated (*rac*)-, (*S*)- and (*R*)-^{18}F-OF-NB1 in rhesus monkeys. The high GluN1/2B specific binding of (*S*)-^{18}F-OF-NB1 (grey matter BP_{ND} values in the range of 1.6-3.5) and its attractive pharmacokinetic profile render it a promising candidate for clinical translation. Clinical PET imaging of GluN1/2B could expedite the development of GluN1/2B therapeutics through target engagement and occupancy studies. Furthermore, PET imaging of diseases in which the GluN2B subunit-containing NMDARs are implicated could potentially improve the diagnosis and treatment monitoring of these diseases.

ACKNOWLEDGMENTS

The authors thank the staff at the Yale PET Center for their expert technical support.

DISCLOSURE

H. A., S. M. A. and A. H. hold shares in Nemosia A.G. No other potential conflicts of interest relevant to this article exist.

KEY POINTS

QUESTION: Can we selectively image GluN2B subunit-containing NMDARs in NHPs, and identify a suitable radiofluorinated PET probe for clinical translation?

PERTINENT FINDINGS: (*S*)-^{18}F-OF-NB1 emerged as an attractive candidate for clinical translation, as it displayed high specific binding to GluN1/2B receptors and favorable pharmacokinetic profile.

IMPLICATIONS FOR PATIENT CARE: A GluN1/2B PET tracer suitable for use in human will facilitate the investigation and diagnosis of neuropsychiatric diseases, as well as the development of therapeutics targeting GluN2B-containing NMDA receptors.

REFERENCES

1. Hansen KB, Yi F, Perszyk RE, et al. Structure, function, and allosteric modulation of NMDA receptors. *J Gen Physiol.* 2018;150:1081-1105.

2. Hardingham GE, Bading H. Synaptic versus extrasynaptic NMDA receptor signalling: implications for neurodegenerative disorders. *Nat Rev Neurosci.* 2010;11:682-696.

3. Wang R, Reddy PH. Role of glutamate and NMDA receptors in Alzheimer's Disease. *J Alzheimers Dis.* 2017;57:1041-1048.

4. Paoletti P, Bellone C, Zhou Q. NMDA receptor subunit diversity: impact on receptor properties, synaptic plasticity and disease. *Nat Rev Neurosci.* 2013;14:383-400.

5. Adell A. Brain NMDA receptors in schizophrenia and depression. *Biomolecules.* 2020;10;947.

6. Ahmed H, Haider A, Ametamey SM. N-Methyl-D-Aspartate (NMDA) receptor modulators: a patent review (2015-present). *Expert Opin Ther Pat.* 2020;30:743-767.

7. Liu W, Jiang X, Zu Y, et al. A comprehensive description of GluN2B-selective N-methyl-D-aspartate (NMDA) receptor antagonists. *Eur J Med Chem.* 2020;200:112447.

8. Kemp JA, McKernan RM. NMDA receptor pathways as drug targets. *Nat Neurosci.* 2002;5 Suppl:1039-1042.

9. Myers SJ, Ruppa KP, Wilson LJ, et al. A glutamate N-methyl-D-aspartate (NMDA) receptor subunit 2B-selective inhibitor of NMDA receptor function with enhanced potency at acidic pH and oral bioavailability for clinical use. *J Pharmacol Exp Ther.* 2021;379:41-52.

10. Arakawa R, Takano A, Halldin C. PET technology for drug development in psychiatry. *Neuropsychopharmacol Rep.* 2020;40:114-121.

11. Hargreaves RJ, Rabiner EA. Translational PET imaging research. *Neurobiol Dis.* 2014;61:32-38.

12. Fuchigami T, Nakayama M, Yoshida S. Development of PET and SPECT probes for glutamate receptors. *ScientificWorldJournal.* 2015;2015:716514.

13. Cai L, Liow JS, Morse CL, et al. Evaluation of (11)C-NR2B-SMe and its enantiomers as PET radioligands for imaging the NR2B subunit within the NMDA receptor complex in rats. *J Nucl Med.* 2020;61:1212-1220.

14. Krämer SD, Betzel T, Mu L, et al. Evaluation of (11)C-Me-NB1 as a potential pet radioligand for measuring GluN2B-containing NMDA receptors, drug occupancy, and receptor cross talk. *J Nucl Med.* 2018;59:698-703.

15. Mu L, Krämer SD, Ahmed H, et al. Neuroimaging with radiopharmaceuticals targeting the glutamatergic system. *Chimia (Aarau).* 2020;74:960-967.

16. Haider A, Herde AM, Krämer SD, et al. Preclinical evaluation of benzazepine-based PET radioligands (R)- and (S)-(11)C-Me-NB1 reveals distinct enantiomeric binding patterns and a tightrope walk between GluN2B- and σ(1)-receptor-targeted PET imaging. *J Nucl Med.* 2019;60:1167-1173.

17. Rischka L, Vraka C, Pichler V, et al. First-in-human brain PET imaging of the GluN2B-containing N-methyl-D-aspartate receptor with (R)-11C-Me-NB1. *J Nucl Med.* 2021;In press.

18. Haider A, Iten I, Ahmed H, et al. Identification and preclinical evaluation of a radiofluorinated benzazepine derivative for imaging the GluN2B subunit of the ionotropic NMDA receptor. *J Nucl Med.* 2019;60:259-266.

19. Ahmed H, Wallimann R, Haider A, et al. Preclinical development of (18)F-OF-NB1 for imaging GluN2B-containing N-methyl-D-aspartate receptors and its utility as a biomarker for amyotrophic lateral sclerosis. *J Nucl Med.* 2021;62:259-265.

20. Zheng M, Ahmed H, Smart K, et al. Characterization in nonhuman primates of (R)-[(18)F]OF-Me-NB1 and (S)-[(18)F]OF-Me-NB1 for imaging the GluN2B subunits of the NMDA receptor. *Eur J Nucl Med Mol Imaging.* 2022;In press.

21. Wilson AA, Jin L, Garcia A, DaSilva JN, Houle S. An admonition when measuring the lipophilicity of radiotracers using counting techniques. *Appl Radiat Isot.* 2001;54:203-208.

22. Cai Z, Li S, Zhang W, et al. Synthesis and preclinical evaluation of an (18)F-labeled synaptic vesicle glycoprotein 2A PET imaging probe: [(18)F]SynVesT-2. *ACS Chem Neurosci.* 2020;11:592-603.

23. Barta-Szalai G, Borza I, Bozó E, et al. Oxamides as novel NR2B selective NMDA receptor antagonists. *Bioorg Med Chem Lett.* 2004;14:3953-3956.

24. James ML, Shen B, Zavaleta CL, et al. New positron emission tomography (PET) radioligand for imaging σ-1 receptors in living subjects. *J Med Chem.* 2012;55:8272-8282.

25. Li S, Zheng MQ, Naganawa M, et al. Development and in vivo evaluation of a κ-opioid receptor agonist as a PET radiotracer with superior imaging characteristics. *J Nucl Med.* 2019;60:1023-1030.

26. Zheng MQ, Nabulsi N, Kim SJ, et al. Synthesis and evaluation of 11C-LY2795050 as a κ-opioid receptor antagonist radiotracer for PET imaging. *J Nucl Med.* 2013;54:455-463.

27. Hilton J, Yokoi F, Dannals RF, Ravert HT, Szabo Z, Wong DF. Column-switching HPLC for the analysis of plasma in PET imaging studies. *Nucl Med Biol.* 2000;27:627-630.

28. Ichise M, Toyama H, Innis RB, Carson RE. Strategies to improve neuroreceptor parameter estimation by linear regression analysis. *J Cereb Blood Flow Metab.* 2002;22:1271-1281.

29. Cunningham VJ, Rabiner EA, Slifstein M, Laruelle M, Gunn RN. Measuring drug occupancy in the absence of a reference region: the Lassen plot re-visited. *J Cereb Blood Flow Metab.* 2010;30:46-50.

30. Pike VW. PET radiotracers: crossing the blood-brain barrier and surviving metabolism. *Trends Pharmacol Sci.* 2009;30:431-440.

31. Shen Z, Lv C, Zeng S. Significance and challenges of stereoselectivity assessing methods in drug metabolism. *J Pharm Anal.* 2016;6:1-10.

32. Smart K, Zheng MQ, Ahmed H, et al. Comparison of three novel radiotracers for GluN2B-containing NMDA receptors in non-human primates: (R)-[(11)C]NR2B-Me, (R)-[(18)F]of-Me-NB1, and (S)-[(18)F]of-NB1. *J Cereb Blood Flow Metab.* 2022;In press.

33. Guo Q, Owen DR, Rabiner EA, Turkheimer FE, Gunn RN. A graphical method to compare the in vivo binding potential of PET radioligands in the absence of a reference region: application to [^{11}C]PBR28 and [^{18}F]PBR111 for TSPO imaging. *J Cereb Blood Flow Metab.* 2014;34:1162-1168.

34. Ryskamp DA, Korban S, Zhemkov V, Kraskovskaya N, Bezprozvanny I. Neuronal sigma-1 receptors: signaling functions and protective roles in neurodegenerative diseases. *Front. Neurosci.* 2019;13:862.

35. Pabba M, Wong AY, Ahlskog N, et al. NMDA receptors are upregulated and trafficked to the plasma membrane after sigma-1 receptor activation in the rat hippocampus. *J Neurosci.* 2014;34:11325-11338.

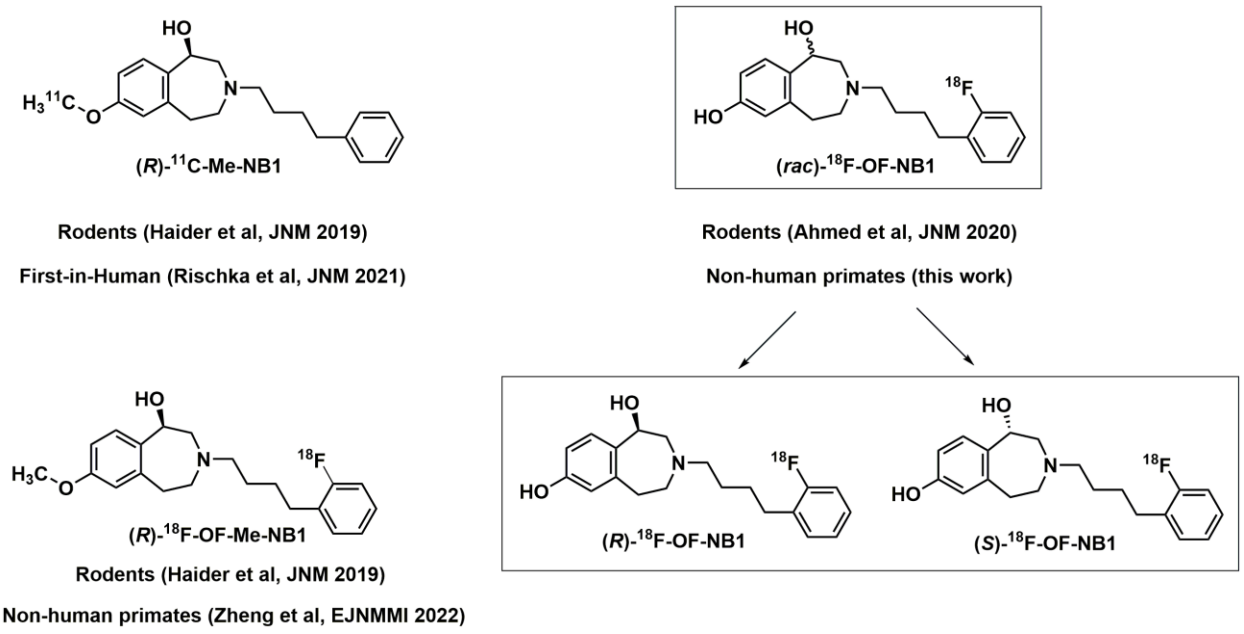

Figure 1: Structures of (*R*)-^{11}C-Me-NB1, the lead radiotracer recently evaluated in a clinical trial, (*R*)-^{18}F-OF-Me-NB1, the first radiofluorinated derivative of (*R*)-^{11}C-Me-NB1 evaluated in rats, and (*rac*)-, (*R*)-, and (*S*)- and ^{18}F-OF-NB1 evaluated in the current work.

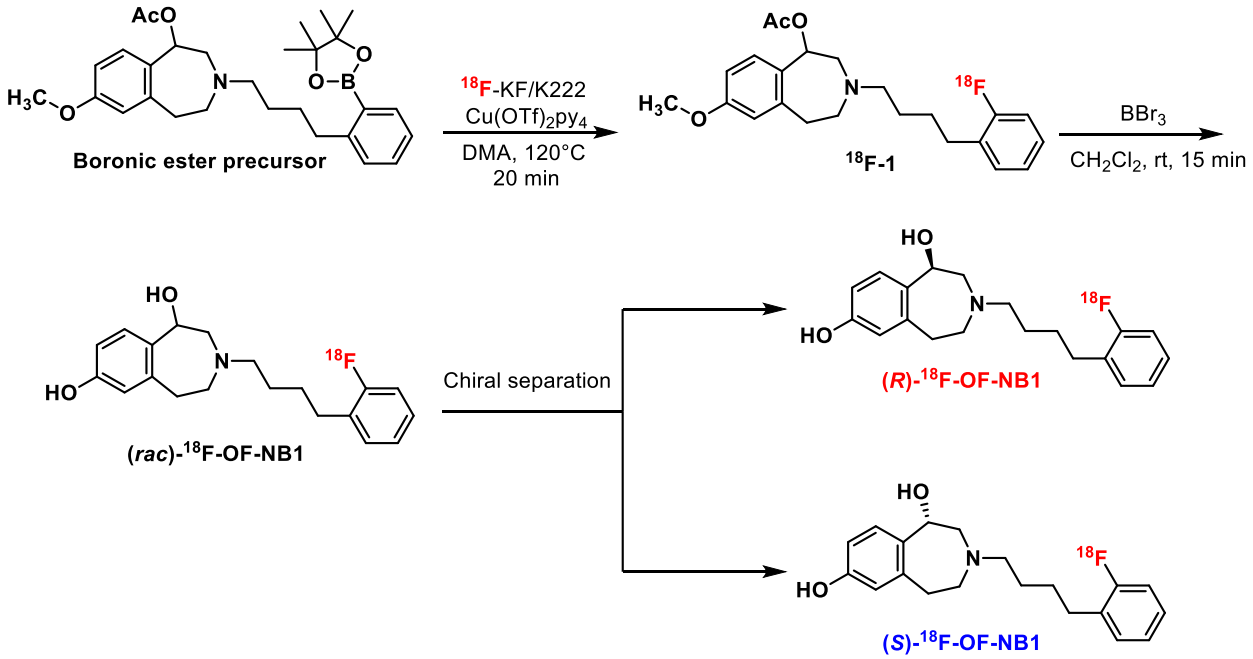

Figure 2: Radiosynthesis of (*rac*)-, (*R*)-, and (*S*)-^{18}F-OF-NB1.

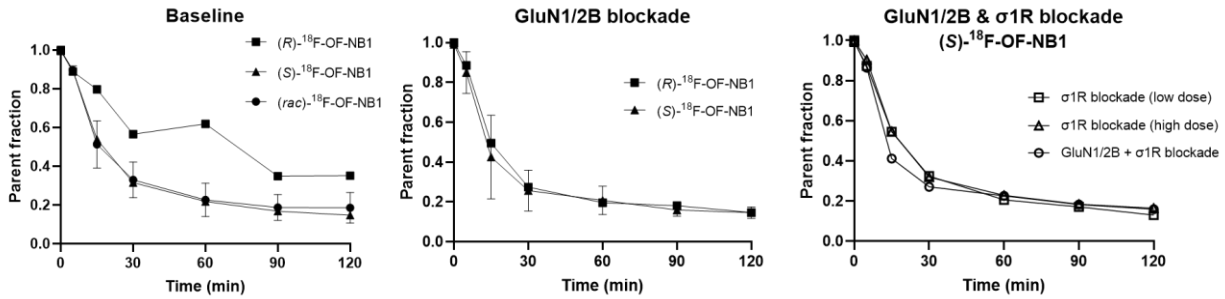

Figure 3: Parent fraction remaining of (*rac*)-, (*R*)- and (*S*)-^{18}F-OF-NB at different time points under baseline and blockade conditions. For GluN1/2B blockade, a dose of 0.25 mg/kg of Co 101244 was used. For σ_1R blockade, either a low (0.027 mg/kg) or high dose (0.125 mg/kg) of FTC-146 was used.

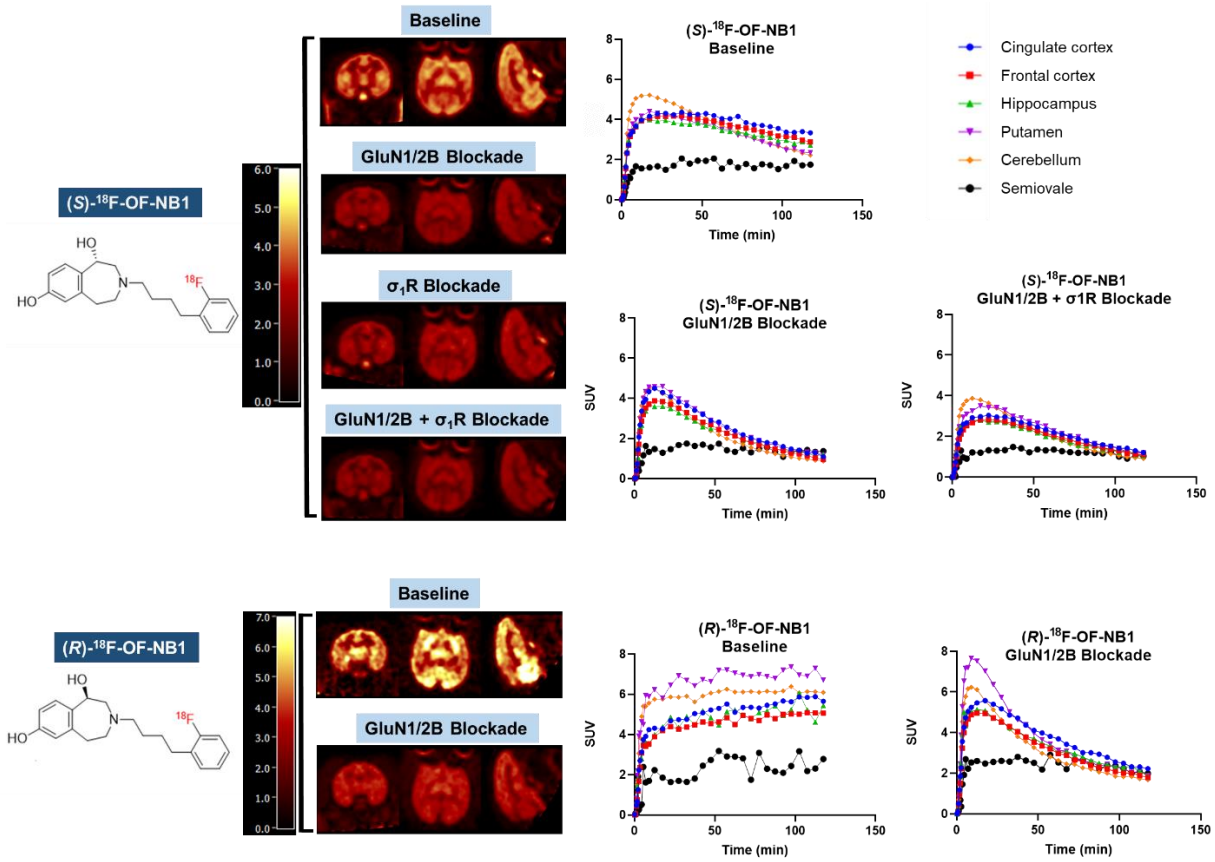

Figure 4: Top panel: Representative PET SUV images (summed from 45-60 min) and time-activity curves in selected brain regions from the baseline, GluN1/2B blockade (0.25 mg/kg of Co 101244), σ_1R blockade (0.125 mg/kg of FTC-146) and sequential GluN1/2B/σ_1R blockade (0.25 mg/kg Co 101244 + 0.125 mg/kg FTC-146) scans of (*S*)-^{18}F-OF-NB1 obtained in the same rhesus monkey (monkey#2). Bottom panel: PET SUV images and time-activity curves from the baseline and GluN1/2B blockade (0.25 mg/kg Co 101244) scans of (*R*)-^{18}F-OF-NB1 (monkey#1).

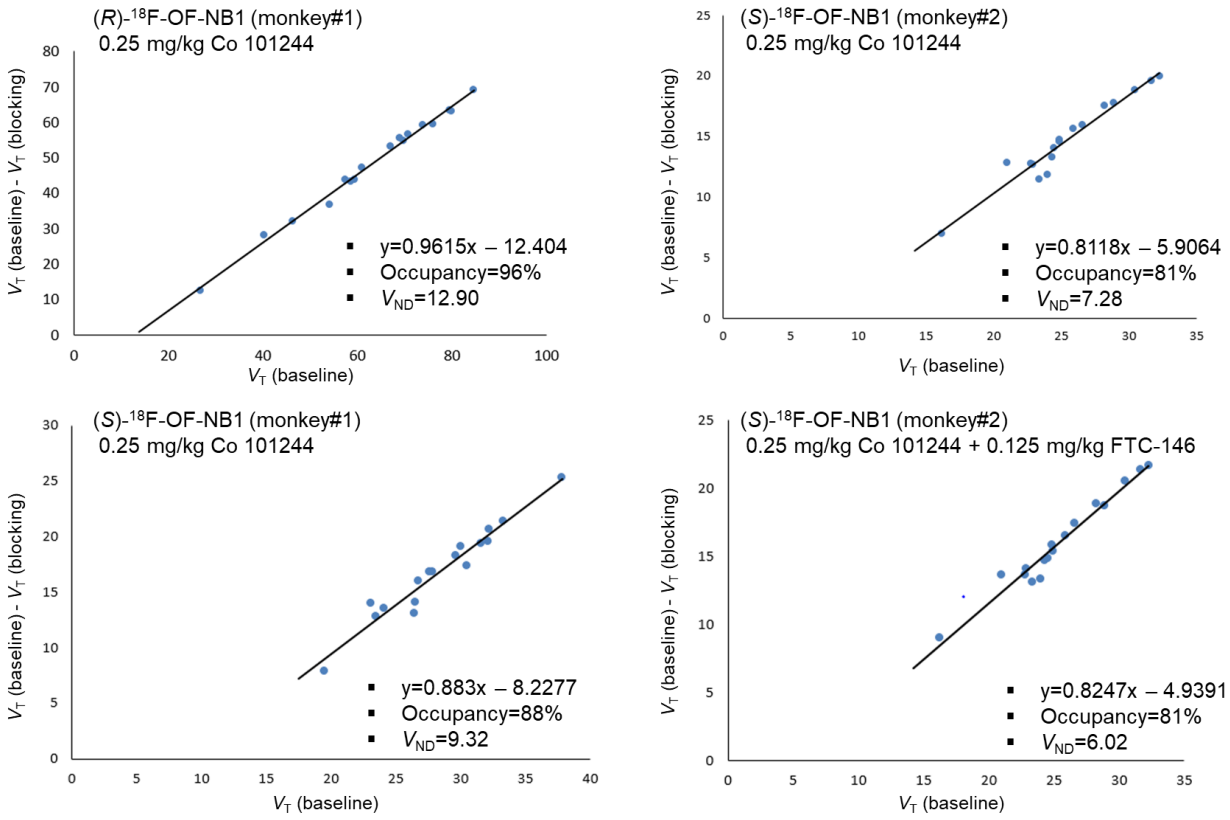

Figure 5: Lassen occupancy plots of (*R*)- and (*S*)-^{18}F-OF-NB1 following pretreatment with either the GluN1/2B ligand Co 101244 (0.25 mg/kg) only or with the addition of the σ_1R ligand FTC-146 (0.125 mg/kg). Each point represents a unique brain region.

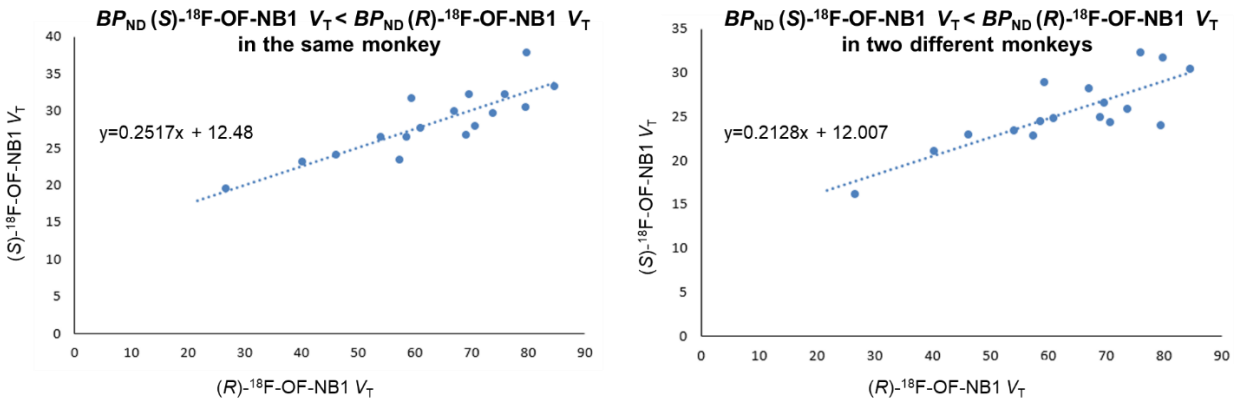

Figure 6: Guo plots comparing the regional V_T values of (*S*)-^{18}F-OF-NB1 (Y-axis) and (*R*)-^{18}F-OF-NB1 (X-axis) in the same monkey (Left) and in two different monkeys (Right). The Y-intercept is > 0, signifying higher BP_{ND} values of the tracer on the X-axis than the one on the Y-axis. The slope indicates the relative *in vivo* binding affinity of the two tracers where (*R*)-^{18}F-OF-NB1 exhibits four to five-fold higher binding affinity than the (*S*)-enantiomer.

Table 1: 1TCM V_T and BP_{ND} values of (*S*)-^{18}F-OF-NB1 in selected brain regions under baseline and blockade conditions in two different monkeys, and those in parenthesis for (*R*)-^{18}F-OF-NB1 in one monkey. V_{ND} values were derived from the GluN1/2B blocking scan using Co 101244.

	V_T (mL/cm^3)						**BP_{ND}**	
Region of interest	**Baseline**		**Co 101244 (0.25 mg/kg)**		**FTC-146 (0.027 mg/kg)**	**FTC-146 (0.125 mg/kg)**	$(V_T - V_{ND})/V_{ND}$	
	Monkey#1	Monkey#2	Monkey#1	Monkey#2	Monkey#1	Monkey#2	Monkey#1	Monkey#2
Thalamus	24.6 (39.6)	23.3	10.4 (13.7)	10.2	20.9	13.9	1.64 (2.1)	2.20
Cerebellum	27.3 (50.3)	25.5	10.8 (13.1)	10.2	19.6	15.5	1.93 (2.9)	2.50
Cingulate cortex	38.8 (59.5)	32.3	12.6 (16.5)	12.1	27.9	19.3	3.16 (3.6)	3.44
Frontal cortex	31.1 (49.1)	28.9	11.0 (13.8)	10.7	20.9	17.3	2.34 (2.8)	2.97
Hippocampus	32.1 (50.8)	26.3	11.5 (14.6)	10.6	24.0	16.2	2.44 (2.9)	2.61
Semiovale	20.3 (30.9)	16.9	10.6 (13.7)	9.0	15.9	11.5	1.18 (1.4)	1.32

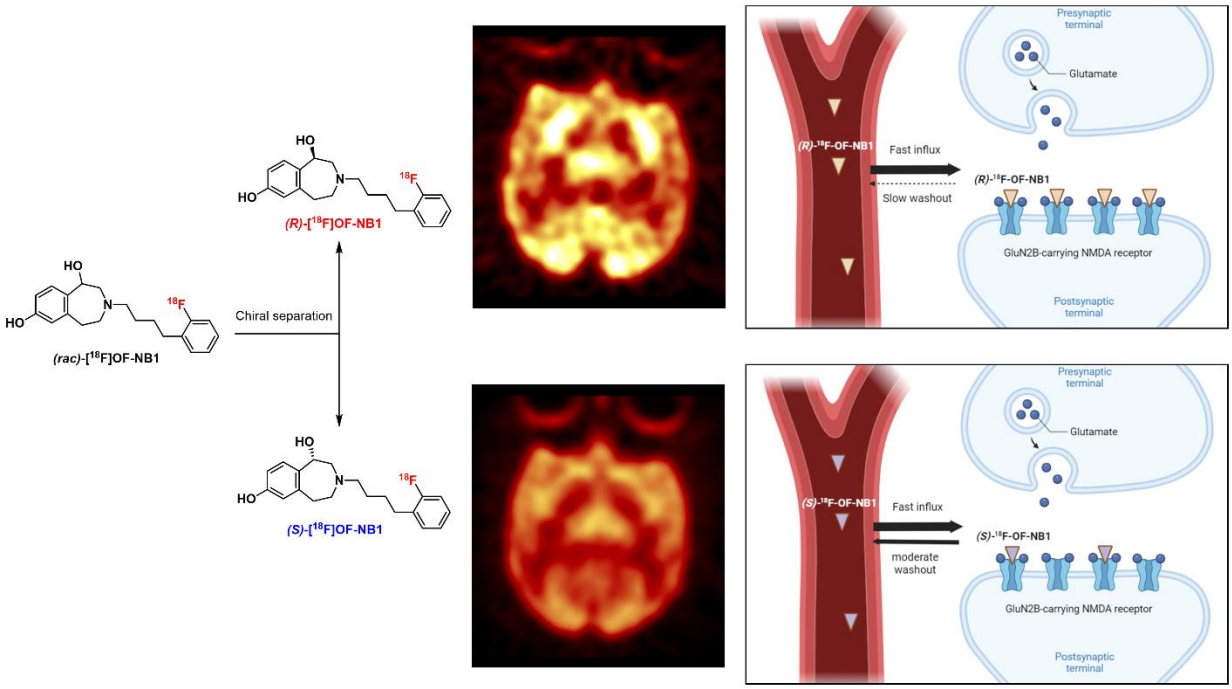

Graphical Abstract

Supplemental material for

Evaluation of (*rac*)-, (*R*)- and (*S*)-^{18}F-OF-NB1 for imaging GluN2B subunit-containing *N*-methyl-*D*-aspartate receptors in non-human primates

Hazem Ahmed[1, 2*], Ming-Qiang Zheng[2*], Kelly Smart[2], Hanyi Fang[2, 3], Li Zhang[2], Paul R. Emery[2], Hong Gao[2], Jim Ropchan[2], Ahmed Haider[1], Gilles Tamagnan[2], Richard E. Carson[2], Simon M. Ametamey[1†], Yiyun Huang[2†]

1. Institute of Pharmaceutical Sciences, ETH Zurich, Zurich, Switzerland

2. PET Center, Yale University, New Haven, Connecticut, USA

3. Union Hospital, Huazhong University of Science and Technology, Wuhan, China

* Both authors contribute equally to this work

†Corresponding authors

- Prof. Yiyun Henry Huang, PO Box 208048, PET Center, Yale School of Medicine, 801 Howard Ave, New Haven, CT 06520-8048, USA, Tel: 203-785-3605, e-mail: henry.huang@yale.edu

- Prof. Simon M. Ametamey, Institute of Pharmaceutical Sciences, ETH Zurich, Zurich, Switzerland e-mail: simon.ametamey@pharma.ethz.ch

PET Imaging in Rhesus Monkeys

Anesthesia in animals was induced using a mixture of alfaxalone (2 mg/kg), midazolam (0.3 mg/kg) and dexmedetomidine (0.01 mg/kg), and maintained afterwards with 1.5-2.5% isoflurane in oxygen using endotracheal intubation. Vital signs (heart rate, blood pressure, respiration rate, and oxygen saturation) were monitored continuously during the scan using a physiological monitor. The body temperature was maintained using a water-jacket heating pad. Blood sampling was performed using an arterial line that was placed in the radial artery. Radiotracer solution (10 mL) was administered intravenously over 3 min using an infusion pump (PHD 22/ 2000; Harvard Apparatus). Emission data were acquired in list mode for 120 min. Subsequently, these data were binned into successive frames of increasing durations (6 × 30 s, 3 × 1 min, 2 × 2 min, 22 × 5 min).

Image processing. For the purpose of region of interest (ROI) definition, high resolution magnetic resonance images were recorded using a Siemens 3T Trio scanner. A 9 min transmission scan was performed for attenuation correction prior to radiotracer injection. The PET emission data were also corrected for scanner normalization, scatter, and randoms. The corrected PET emission data was reconstructed using a Fourier rebinning and filtered by a back-projection algorithm. Averaged PET images for the first 10 min of each scan were matched to the anatomical MR image, and inverted transformations were applied in order to superimpose the PET image to an atlas ROI mask of a rhesus monkey. Time-activity curves were then generated from each defined ROI.

HPLC column switching method. Plasma samples were treated with urea (8 M) to eliminate plasma protein binding, and loaded onto the capture column (19 × 4.6 mm) self-packed with Phenomenex SPE C18 Strata-X sorbent and eluting with 1% acetonitrile in water at a flow rate of 2 mL/min. After 4 min, activity trapped on the capture column was back-eluted onto the analytical column (Luna C18 column, 250 × 4.6 mm, 5 μm) using 45% acetonitrile in 0.1 M ammonium formate at a flow rate of 1.5 mL/min.

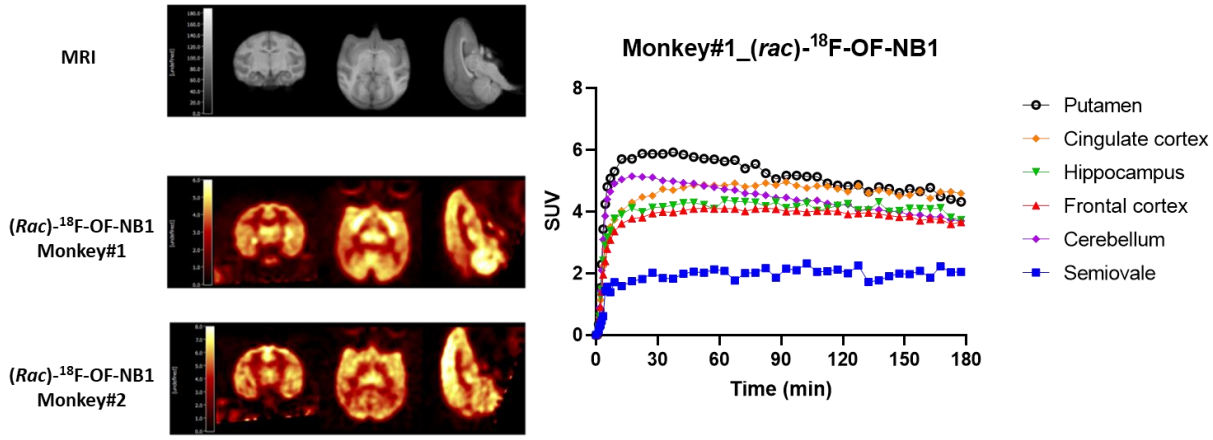

Supplemental Figure 1: Left: MR (top) and PET SUV images summed from 45-60 min after injection of (*rac*)-^{18}F-OF-NB1 in two rhesus monkeys. Right: Time-activity curves of representative brain regions from the baseline scan of (*rac*)-^{18}F-OF-NB1 in monkey#1

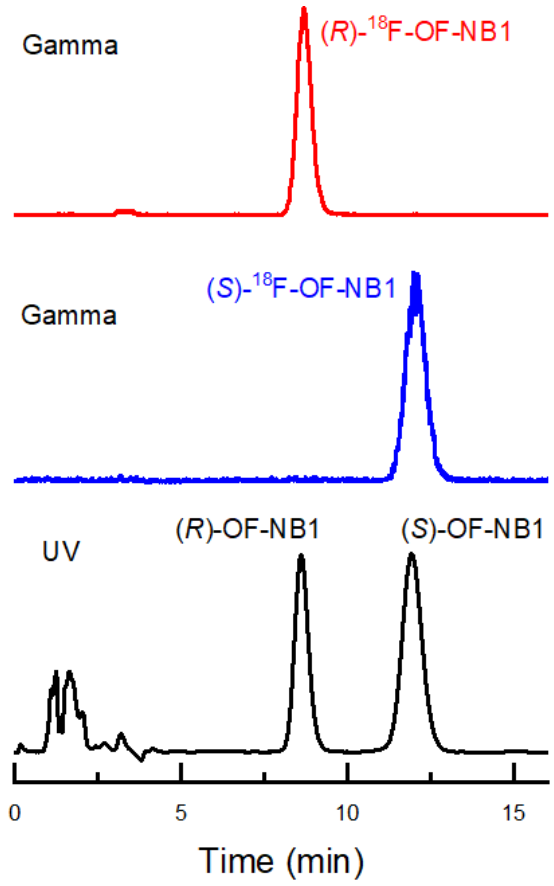

Supplemental Figure 2: Gamma chromatograms from chiral HPLC analysis of the formulated enantiopure radiotracers, together with UV chromatogram of the racemic reference. The following chiral HPLC column and conditions were used for analysis: Regis C-Amylose A column (250 x 4.6 mm, 3 µm); mobile phase: 40/60 acetonitrile/0.05% triethylamine in water; flow rate: 2 mL/min.

Supplemental Table 1. Baseline 1TCM V_T values (mL/cm^3) for each form of ^{18}F-OF-NB1 in all examined brain regions of three different animals

Brain region	**(*Rac*)-^{18}F-OF-NB1**		**(*R*)-^{18}F-OF-NB1**	**(*S*)-^{18}F-OF-NB1**	
	*Monkey **1***	*Monkey **3***	*Monkey **1***	*Monkey **1***	*Monkey **2***
Amygdala	45.8	31.6	35.5	23.8	20.4
Brainstem	56.0	28.1	48.5	30.2	26.0
Caudate	52.5	28.9	50.3	28.8	25.0
Cerebellum	50.2	26.9	50.3	27.3	25.5
Cingulate cortex	72.9	39.8	59.5	38.8	32.3
Frontal cortex	57.3	32.6	49..1	31..1	28.9
Globus pallidus	50.0	22.2	35.3	28.2	23.6
Hippocampus	59.0	30.8	50.8	32.1	26.3
Insular cortex	66.3	34.0	56.1	34.7	31.1
Nucleus accumbens	64.9	33.2	60.5	34.2	32.8
Occipital cortex	43.0	25.4	42.2	24.1	23.3
Pons	60.2	29.2	48.8	32.6	29.3
Putamen	60.5	28.2	61.3	31.8	24.6
Centrum semiovale	33.7	16.6	31.0	20.3	16.9
Substantia nigra	52.5	24.8	41.2	27.4	24.9
Temporal cortex	52.2	28.3	45.6	28.8	25.5
Thalamus	44.2	29.6	39.6	24.6	23.3

Supplemental Table 2**.** Baseline MA1 V_T values for each form of ^{18}F-OF-NB1 in all examined regions of three different animals

Brain region	**(*Rac*)-^{18}F-OF-NB1**		**(*R*)-^{18}F-OF-NB1**	**(*S*)-^{18}F-OF-NB1**	
	*Monkey **1***	*Monkey **3***	*Monkey **1***	*Monkey **1***	*Monkey **2***
Amygdala	49.0	32.4	40.30	23.1	21.00
Brainstem	59.6	29.7	73.8	29.6	25.9
Caudate	55.5	31.0	70.8	27.9	24.3
Cerebellum	54.9	28.3	69.1	26.8	24.9
Cingulate cortex	74.7	41.9	79.9	37.9	31.7
Frontal cortex	60.1	34.2	67.1	30.0	28.2
Globus pallidus	52.5	23.0	54.1	26.4	23.4
Hippocampus	64.5	33.5	69.7	32.2	26.6
Insular cortex	69.4	35.3	84.6	33.3	30.5
Nucleus accumbens	68.1	34.7	76.0	32.2	32.3
Occipital cortex	46.1	26.7	57.5	23.4	22.8
Pons	63.3	31.4	59.4	31.6	28.9
Putamen	64.2	29.3	79.6	30.5	24.0
Centrum semiovale	35.7	16.8	26.7	19.5	16.2
Substantia nigra	54.7	28.5	58.7	26.5	24.5
Temporal cortex	54.2	29.5	61.0	27.6	24.9
Thalamus	44.7	30.9	46.2	24.1	22.9